ChemSusChem

Research Article
doi.org/10.1002/cssc.202301799

Chemistry Europe
European Chemical Societies Publishing

www.chemsuschem.org

Water-soluble Polypyrrole-Polybis(4-oxy benzene sulfonic acid)phosphazene Composites and Investigation of Their Performance as Cathode Binder in Li-ion Batteries

Halil Duyar,[a] Elif Büşra Çelebi,[a, b] Emre Güney,[a] and Ferda Hacıvelioğlu*[a, b]

Current electric storage systems eagerly focus on high-power and energy-dense Lithium-ion batteries to cope with increasing energy storage demands. Since cathode materials are one of the bottlenecks of these batteries, there is much interest in layered lithium-rich manganese oxide-based (LLMO) cathodes which can develop this technology. However, Initial Coulombic Efficiency (ICE) loss, poor rate performance and cycling instability issues are still persistent as problems to be solved for these materials. Recent research shows that water-soluble binders are effective in improving the performance of LLMO materials. Herein, we describe the synthesis, characterisation, and application of a series of water-soluble composites as a binder for LLMO cathodes. The PPy is introduced as part of the binder to improve the electronic conductivity and two different oxidants and various PPy to PSAP ratios were used to optimise the final properties. The electrochemical performance and morphology of the cathodes before and after cycling were investigated and compared with the conventional PVDF binder. The LLMO−2c electrode showed excellent charge-discharge performance, especially at 5 C and 10 C rates, and high cycling stability at 0.2 C whilst maintaining a final capacity of 184 mAh/g after 200 cycles, which is equal to 89.3 % capacity retention.

Introduction

The increasing demand for storing electrical power in high-energy-density electrochemical devices enforces research activities to focus on lithium-ion batteries (LIBs). Especially, there is an urgent desire for LIBs to power electric vehicles to alter the environmentally polluting fossil fuels. Among the other traditional cathode materials such as $LiNiMnCoO_2$ (NMC), and $LiNiCoAlO_2$ (NCA), layered lithium-rich manganese-based metal oxides (LLMO) [$xLi_2MnO_3.(1\text{-}x)LiMO_2$ (M = transition metal)] have a high theoretical specific capacity (320–350 mAh/g) which can be a solution for the above demand. However, the Li_2MnO_3 structure in these materials decomposes over 4.5 V during charging to release O_2, Li_2O, and manganese and then it turns into the spinel structure by Jahn-Teller distortion which results in initial coulombic efficiency (ICE) loss and cycle instability of LLMOs.[1,2] Besides, poor conductivity of the Li_2MnO_3 in the layered structure of LLMO cathodes results in a low electronic conductivity of the electrode and thus leads to poor rate performance.[3] Although lots of research has been done such as changing the morphological structure,[4] cation doping,[5] anion doping,[6] and metal oxide or polymer coating,[7,8] LLMO cathode materials have not yet emerged commercially.[9] Recently, some attempts have been made to address the aforementioned drawbacks for LLMOs by using different water-soluble binders that facilitate ionic conduction, such as sodium carboxymethyl cellulose (CMC–Na),[10] guar gum (GG),[11] sodium alginate (SA),[12] xanthan gum (XG)[13] and poly(acrylic acid) lithium salt (PAA–Li),[14] instead of the conventional insulating PVDF binder. Implementing these novel binders was expected to provide better electrochemical performance by improving the stability of electrodes and thus suppress the capacity fade during cycling.[10] Moreover, removing the harmful and toxic N-methyl-2-pyrrolidone used for dissolving the PVDF binder from the manufacturing process makes battery fabrication simpler, cheaper, and environmentally friendly. On the other hand, LLMO-based cathode materials usually have a wide electrochemical window of 2.0 to 4.8 V which forces the binders to meet higher requirements, including excellent electrochemical stability and low charge transfer resistance at such a high working voltage range. Furthermore, it is also expected that a binder to provide good adhesion to the electrode surface and the cathode material whilst providing good electrical conductivity. Hence, it is necessary to develop alternative binders not only for LLMO-based cathode materials to overcome the capacity fade and cycling instability issues but also for the other electrode materials for environmental concerns.

Intrinsically conducting polymers (ICPs) have drawn considerable attention in recent decades due to their diverse

[a] H. Duyar, Dr. E. Büşra Çelebi, E. Güney, Prof. Dr. F. Hacıvelioğlu
Department of Chemistry
Gebze Technical University,
41400, Gebze, Kocaeli
E-mail: halilduyar@gtu.edu.tr
ebcelebi@gtu.edu.tr
e.guney2020@gtu.edu.tr
ferda@gtu.edu.tr

[b] Dr. E. Büşra Çelebi, Prof. Dr. F. Hacıvelioğlu
School of Chemistry
University of Glasgow

Supporting information for this article is available on the WWW under https://doi.org/10.1002/cssc.202301799

structures, flexibility, electroactivity, and adjustable conductivity.[15–18] These features make them more desirable than metals in certain applications. Among the various ICPs, polypyrrole (PPy) is especially promising in certain commercial applications because of its simple preparation, good environmental stability, and high conductivity compared to others.[19–21] PPy has been found to have many potential applications in electrochromic windows, membrane separation, lightweight batteries, solid electrolytic capacitors, sensors, and so on.[22–25] However, some important drawbacks of synthetic conductive PPy are its low solubility, limited mechanical strength, and thus poor binder properties, which is a barrier to its wider usage for battery applications.[18,26,27] Attempts to increase the mechanical and water solubility properties of PPy by implementing polystyrene sulfonic acid (PSS) polyelectrolyte as a counter ion were successful.[28,29] However, the PSS is prone to degradation under oxidative conditions and thus it is inevitable to result in chain scission reactions during the operating battery conditions.[30–32] Among the different sulfonic acid-carrying polymers, sulfonic acid substituted polyaryloxyphosphazenes can be a viable alternative as an anionic counter ion for ICPs to enhance the solubility, conductivity, mechanical properties and thus processability.[33,34] Polyphosphazenes have alternating phosphorus and nitrogen atoms on their main chain where two side groups are linked to the phosphorus atom. Thus, the P and N atoms are in their highest oxidation states which makes them resistive to chemical and thermal oxidative conditions.[35,36] It is known that the addition of alkoxy functional cyclic phosphazene derivatives increases the thermal stability of the electrolyte whilst fluorinated alkoxy analogues can bind Li^+ cations on their structure helping to mass transfer during charge-discharge cycles.[37–39] Besides, phosphazene-based ionic conductors can also suppress the dendrite growth in LIBs.[40] Hence, phosphazenes have more unique advantages compared to organic analogues for LIB applications. An attractive high-yield pathway to sulfonic acid functional polyaryloxyphosphazenes has been recently developed by some of us which made the fully sulfonated polybis(4-oxybenzene sulfonic acid)phosphazene (PSAP) easily accessible by simple synthetic chemistry.[41] Thus, all these unique features, *i.e.*, thermal, oxidative, photochemical stability, and fire retardancy properties make the PSAP an attractive alternative to PSS as a solubility enhancer for PPy.

In the current study, we have successfully prepared different compositions of PSAP with PPy by using the chemical oxidation polymerization of pyrrole. The stoichiometry of the pyrrole monomer was adjusted from 0.5 to 1.5 against the constant amount (1 eq.) of the counter anion PSAP polyelectrolyte. The structural properties of new materials were investigated by standard spectroscopic techniques. Thermal, morphologic, and conductivity properties of the composites were also investigated and compared to the pristine PPy. Then the best composite materials in terms of electrical conductivity, and thermal stability were used as an alternative binder to build LLMO-based cathode material which is prepared by the sol-gel method as described in the literature.[42] The prepared cathode materials were used to build 2032-coin cells and then cycling stability and charge-discharge characteristics were investigated and compared with the cathode electrode prepared with the conventional PVDF binder.

Results and Discussion

We have previously reported the synthesis of $Cl_3P{=}NSiMe_3$ monomer from readily available and cheap chemicals under mild conditions which is used to prepare the starting polymer for this work.[43] Therefore, the polydichlorophosphazene (PDCP) was synthesized from $Cl_3P{=}NSiMe_3$ monomer by using the PCl_5 as initiator and then reacted with ethyl 4-hydroxybenzenesulfonate. The resulting polyphosphazene intermediate is subsequently converted into the sulfonic acid form, purified by dialysis, and dried in a vacuum oven to give the polybis(4-oxybenzene sulfonic acid)phosphazene (PSAP) polyelectrolyte.[41] Then, a known amount of PSAP was dissolved in water and three different stoichiometric ratios of pyrrole (PSAP/Pyrrole; 1:0.5, 1:1, 1:1.5) were fed into the PSAP solutions to obtain PSAP/PPy composites under chemical oxidative polymerization conditions where ammonium or sodium peroxydisulfate (APS or NaPS) were oxidants (Scheme 1).

The obtained materials including PPy, PSAP and PPy/PSAP composites were analysed with standard spectroscopic technics and all the results were consistent within the given polymer compositions. Especially the FT-IR spectra were carefully analysed to investigate the functional groups and interactions between the PPy and PSAP in **1a–c** and **2a–c** (Figure 1). The characteristic peaks of PSAP observed at 1590 and 1490 cm^{-1} were assigned to aromatic C=C stretching vibrations, whilst the P=N and P–N stretching were observed at 1214 and 1121 cm^{-1}, respectively. The S=O and S–O stretching vibrations arising from the sulfonic acid functionality can be detected at 1038 and 1008 cm^{-1} and P–O–C antisymmetric stretching is observed at 935 cm^{-1} which is an indication of phenol substitution to the polyphosphazene backbone. The PPy has its characteristics peaks at 797&932 cm^{-1} and 1050 cm^{-1} which can be attributed to C–H wagging, and C–H in-plane deformation vibrations. The peaks at 1215 cm^{-1} and 1286 cm^{-1} represent the C–N stretching and C–H in-plane vibration respectively. Also, the peak at 1675 cm^{-1} can be attributed to the ring stretching mode of PPy.[45,46] The **1a–c** and **2a–c** composites have all the peak motifs of the parent compounds PPy and PSAP. In addition, the

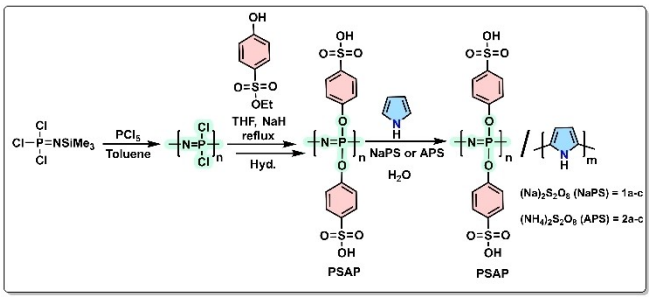

Scheme 1. Overall scheme for the synthesis of **1a–c**&**2a–c** composites.

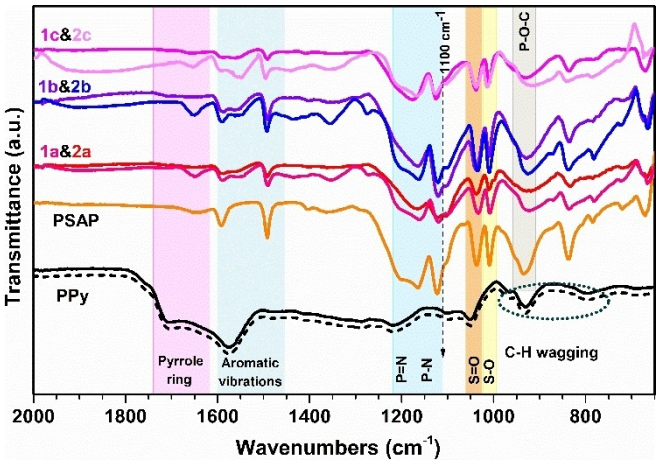

Figure 1. FT-IR spectra of PPy, PSAP, **1a–c** and **2a–c**.

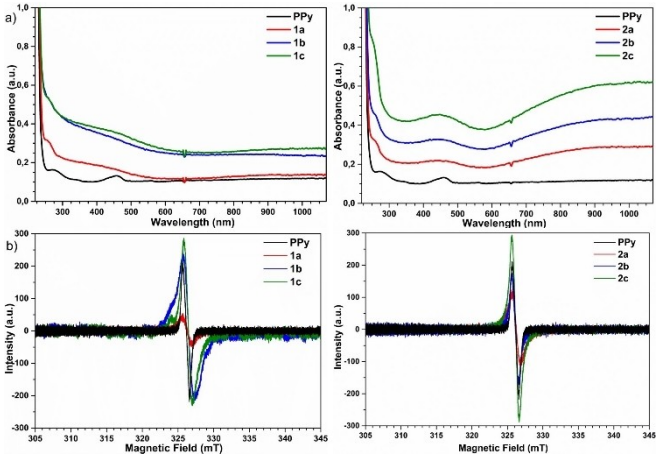

Figure 2. Comparative a) UV–Vis and b) complimentary EPR spectra of the PPy and **1a–c**&**2a–c**.

peak at 1100 cm^{-1} represents the S=O stretching vibration of sulfonate anions, $-SO_3^-$, which compensates for the positive charges on the PPy.[46]

The interaction of PPy with PSAP was also clear in the ^1H NMR spectra (Figure S1). As seen the PSAP has two broad peaks at $\delta = 6.55$ and 7.35 ppm which were assigned to the p-substituted aromatic phenol ring protons. On the other hand, the representative examples of PPy/PSAP, *i.e.*, **1b** and **2b**, have new peaks, which are necking near the PSAP aromatic peaks, at $\delta = 6.70$ and 7.55 ppm are assigned to the proton resonance of the p-substituted phenol ring interacting with the PPy over the sulfonic acid moieties. Unfortunately, the proton resonances of the PPy ring on PPy/PSAP composites could not be detected at the aromatic region of the spectrum due to the Knight-Shift.[47] Furthermore, the ^{31}P NMR was also supporting the interaction of PPy with PSAP. The ^{31}P NMR spectrum of PSAP consist of only one broad peak at $\delta = -20.11$ ppm arising from the phosphorus atoms of the polyaryloxyphosphazene backbone. The peak becomes broader in the PPy/PSAP macromolecular salt systems which further indicates that the PSAP is interacting with PPy (Figure S1).

The electronic properties of PPy/PSAP macromolecular salt systems (**1a–c**&**2a–c**) were investigated by UV–Vis and complimentary EPR measurements (Figure 2). Although the oxidation potential of $Na_2S_2O_8$ (NaPS) and $(NH_4)_2S_2O_8$ (APS) is very similar the resulting PPy/PSAP macromolecular salts represent slightly different electronic properties as seen on the UV–Vis spectra (Figure 2a&b). The strong broad absorption peak at ≤ 300 nm is arising from the π–π^* transition of all the measured materials, and neutral PPy is characterised by the polaron transition around ~450–460 nm.[48] As seen both PPys synthesized by either the presence of NaPS or APS have similar adsorption characteristics and an absorption band at ~456 nm indicating the existence of neutral PPy in their structures.[45] However, the 1a-c samples prepared by NaPS oxidant have a very slight increase in the absorbance intensity by the increasing amount of PPy over 800 nm indicating the presence of polaron transitions. In contrast, the **2a–c** samples prepared by using the APS have more obvious neutral and doped PPy absorbances at ~450 and ~980 nm (Figure 2b). The solid-state EPR spectra were more useful in investigating the presence of half-spin polarons in the oxidised PPy. As seen both **1a–c** and **2a–c** samples have broad EPR signal centred at 326.2 mT ($g = 1.9974$) indicating the presence of polarons in their structures. The integrated EPR results reveal that both the **1a–c** and **2a–c** series have similar polaron concentrations, increasing with the increasing PPy amount in the PPy/PSAP macromolecular salts. Thus, the conjugated PPy has charges on its structure where the PSAP macromolecule balances them as a polymeric counterion in the structure of **1a–c** and **2a–c** series.

The Li_2MnO_3 in the layered structure of LLMO has poor conductivity and therefore the electrical conductivity is an important parameter for the PPy/PSAP materials to provide better battery performance compared to traditional PVDF-based binder. Figure 3a&3b shows the temperature-dependent conductivity (σ_{dc}) results of PPys, **1a–c** and **2a–c** materials. As seen the conductivity of PPy prepared in the presence of NaPS is almost five times higher than the PPy prepared in APS

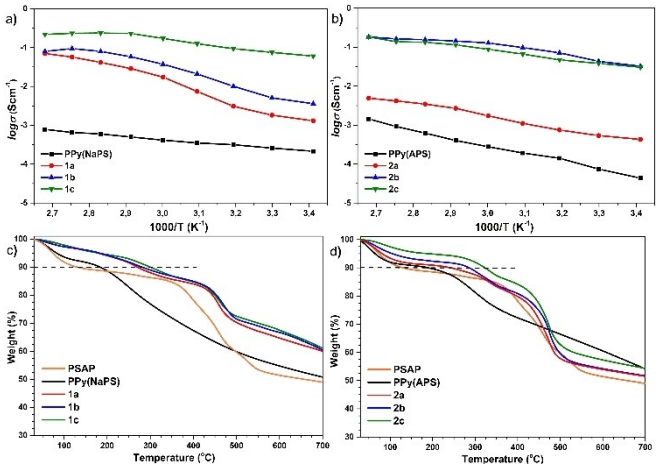

Figure 3. Comparison of a) and b) temperature dependent conductivity and c) and d) TGA results of the PPys, PSAP, **1a–c** and **2a–c** composites.

(Figure 3a&3b and Table 1). However, the situation becomes reversed at 100 °C and the conductivity of PPy (NaPS) (0.8 mS/cm) is lower than PPy prepared in the presence of APS (1.5 mS/cm) at this temperature. The conductivity of **1a–c** and **2a–c** increases by the increasing PPy content and temperature as expected (Figure 3c&3d). The highest conductivity obtained for **1c** was 236 mS/cm at 70 °C and it remains almost constant over this temperature. Unlike the **1a–c** series the conductivity of the **2a–c** series is much more dependent on the temperature but less dependent on the PPy amount in their content. As a result, the conductivity of **2b**&**2c** was very similar and reached the highest value of 185 mS/cm at 100 °C. The thermal stability of **1a–c** and **2a–c** composites was comprehensively examined and compared to PSAP and PPy. TGA results of **1a–c**&**2a–c** composites and polymers were represented in Figure 3c&3d. The PPy, PSAP and their composites have an initial decomposition temperature (T_i) around 100 °C which can be attributed to the expulsion of moisture from the samples.[34] Some of the thermal decomposition results are summarised in Table 1 to make a better comparison. The PSAP is a fully sulfonated polymer and thus shows hygroscopic behaviour. However, it completely loses its humidity around 120 °C and its main decomposition temperature is over 350 °C. As seen from the results in Figure 3c&3d and Table 1, the PPys prepared in the presence of different oxidants, *i.e.*, NaPS or APS, they have slightly different thermal decomposition behaviour. The 10% weight loss temperature (Td_{10}) of PPy(NaPS) was 183 °C and PPy(APS) was 191 °C (Figure 3c&d and Table 1). Interestingly the **1a–c** composites do not show initial water loss behaviour and reach their main decomposition temperature (T_d) over 400 °C by slightly losing their weight which may arise from the desulfation, as the temperature increases. On the other hand, the main decomposition temperature of these composites (**1a–c**) is increasing by the increasing PPy amount in their content and exceeds the T_d of the parent compounds by almost 100 °C. This is probably arising from the ionic interactions between the PPy and PSAP and thus they are forming a tighter structure (Table 1). In the **2a–c** series, the thermal decomposition behaviour is different, and they have similar water loss characteristics to parent PSAP (Figure 3d). Therefore, the PPy starts to decompose over 250 °C which is followed by the decomposition of the PSAP part. Hence, it can be said that the PPy and PSAP formed a tighter structure in their composites and resulted in a more thermally stable final composition compared to parent compounds. This is also reflected to the glass transition temperatures (T_g) of the **1a–c** and **2a–c** materials. Since the PPy is a thermoset polymer, it does not have T_g whilst the PSAP has a T_g of 62 °C.[41] On the other hand, the T_g of the final **1a–c** and **2a–c** compositions increase with the increasing PPy amount in their content (Table 1), thus supporting the TGA findings.

The electronic, thermal, and electrical properties of PPy/PSAP composites are fully characterised above and thus they can be tested as cathode binders in a Li-ion cell. Since these materials have the advantage of electrical conductivity compared to insulating PVDF and therefore the best conducting **1c** and **2c** were selected for this purpose. First, we explored the CV of the cathodes (LLMO−1c, LLMO−2c and LLMO-PVDF) between 2.0 to 4.7 V against the Li reference electrode to understand the reaction kinetics during the ion insertion/desertion process (Figure S2, Supporting Information). The activation of Li_2MnO_3 mostly occurs after the initial anodic scan above 4.5 V for the LLMO cathodes.[10] As can be observed the oxidation of Ni^{2+}&Co^{3+} to higher states (Ni^{4+}&Co^{4+}) takes place at ~4.3 V in the initial forward scan for the LLMO−1c and LLMO−2c cathodes whilst the LLMO-PVDF shows the same oxidations at ~4.1 V (Figure S2) which agrees with the previous reports.[10,11,12,14] Since the conversion of Li_2MnO_3 to the $LiMn_2O_4$ spinel is irreversible, the second and further anodic cycles do not show an extensive current increase over 4.4 V (Figure S2).[10] The formation of the $LiMn_2O_4$ spinel subsequently results in a voltage fade by the gradual occupation of octahedral positions with transition metal ions due to the loss of excess Li ions to electrochemically inactive tetrahedral positions.[49] Therefore, oxidation of Ni^{2+}&Co^{3+} to higher states usually shifts to a lower potential ($\leq$4 V) after the initial cycle. According to Figure S2, the voltage fade of the LLMO−2c and LLMO-PVDF stabilises around ~4.0 V on the second and subsequent cycles. However, the LLMO−1c shows a further left shift on the 3rd cycle for the oxidation of Ni^{2+}&Co^{3+} to higher states at 3.9 V (Figure S2). Thus, probably further loss of Li ions into the inactive tetrahedral positions occurs, resulting in a higher voltage fade

Table 1. Thermal and Conductivity data of the materials.

Sample	Ti[a] (°C)	T10 (°C)	Td (°C)	Yc[b] (%)	Tg (°C)	σ[c]
Ppy(NaPS)	101.0	181.7	180.1	50.8	–	0.21
Ppy(APS)	84.2	188.3	181.3	54.1	–	0.04
PSAP	119.9	127.7	356.8	48.9	62[37]	6.1[37]
1a	–	268.5	411.8	59.9	88	1.31
1b	–	278.6	426.2	60.5	95	3.63
1c	–	297.5	422.4	61.2	103	61.6
2a	113.1	240.9	358.9	51.5	75	0.42
2b	119.8	286.3	368.4	51.7	85	30.8
2c	126.6	323.5	418.1	54.3	92	32.5

[a] initial weight loss temperature. [b] Char yield at 700 °C. [c] Conductivity of samples at room temperature (mS/cm).

and reminding a less stable cathode material. During the cathodic scan, the reduction of Ni^{4+} & Co^{4+} cations in the layered structure takes place between 4.2 V to 3.5 V in the initial and subsequent cycles for all electrodes. The reduction of Mn^{4+} to Mn^{3+} in the spinel phase does not take place in the initial reverse scan as expected but occurs on the 2nd and 3rd cycles at ~3.3 V for the LLMO−1c and LLMO−2c and at ~3.1 V for LLMO-PVDF (Figure S2).[10] The above difference in the reduction potential of Mn^{4+} for LLMO−1c and LLMO−2c versus LLMO-PVDF may seem insignificant (~0.2 V) but it may also be a sign of a significant improvement in electrode performance.[10] The previous studies show that the gradual voltage shift at this cathodic region is an indication of the suppressed spinel phase transformation.[10] Electrochemical impedance spectroscopy (EIS) was also used to investigate the properties of the electrodes and Figure 4 shows the EIS and charge-discharge characteristic of the 2032-coin cells built by using LLMO−1c, LLMO−2c and comparative LLMO-PVDF cathodes. In Figure 4a Nyquist impedance plot of LLMO-PVDF, LLMO−1c and LLMO−2c electrodes is presented and some of the calculated results are summarised in the supporting information file (ESI) by fitting the equivalent circuit (Table S1). A semicircle in the high-frequency region of the Nyquist plot represents the impedance of the cell arising from the bulk resistance, charge transfer and interface resistances and capacitances. An almost straight line in the low-frequency region is attributed to the Warburg element (W_d), responsible for the diffusion of Li-ions in the cathode material. As one can easily recognise the LLMO−2c and LLMO-PVDF electrodes show a similar slope in the low-frequency region whilst LLMO−2c has a smaller semicircle in the high-frequency region of the Nyquist plot. This reveals that the LLMO−2c has a lower impedance (Figure 4a). Further analysis of the Nyquist plot by fitting the equivalent circuit (Figure S3) shows that the charge transfer resistance (R_{ct}) of LLMO-PVDF was 148.0 Ω whilst the LLMO−2c electrode has over six times lower value of 23.95 Ω (Figure 4a & Table S1). On the other hand, the LLMO−1c electrode has a bigger semicircle compared to LLMO−2c in the high-frequency region indicating much more impedance and thus the charge transfer resistance of 92.35 Ω (Figure 4a & Table S1). Moreover, the comparatively lower slope of the Warburg element for LLMO−1c in the low-frequency region indicates a different Li-ion diffusion mechanism than the LLMO−2c and LLMO-PVDF (Figure 4a & Table S1).

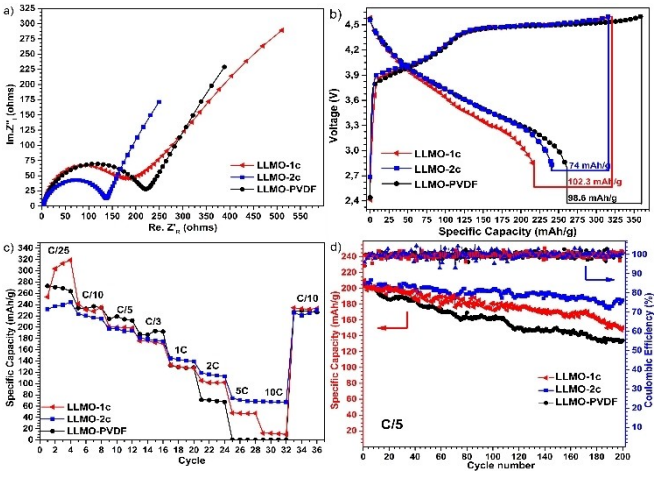

Figure 4. a) Nyquist impedance plot, b) initial capacity-voltage plot, c) capacity retention at different C-rates, and d) cycling test of the cells with different binders.

During the initial oxidation of the cathode, *i.e.*, charging over 4.5 V, the Li_2MnO_3 structure irreversibly transforms into the $LiMn_2O_4$ spinel structure as we have already seen by the electrochemical measurements (Figure S2). This irreversible oxidation then causes a decrease in ICE.[50] The **1c**&**2c** materials have conductive PPy as part of the binder; thus, the electrochemical performance of the electrodes was expected to be better than the traditional PVDF-based binder. The ICE loss of the cathode prepared with PVDF binder was slightly better (Δ = 3.7 mAh/g) and it showed a lower ICE loss of 98.6 mAh/g compared to the cathode prepared with **1c** binder (102.3 mAh/g) (Figure 4b). In contrast, the LLMO−2c cathode showed very good capacity retention in the first cycle with only an ICE loss of 74 mAh/g, surpassing the performance of LLMO-PVDF and LLMO−1c (Figure 4b). The effect of the charge/discharge rate on the electrode performance is given in the galvanostatic charge/discharge (GCD) curves in the supporting information file (Figure S4). According to GCD and capacity retention results of these three electrodes at different C-rates, the LLMO-PVDF cathode shows good charge-discharge stability when it is slowly charged-discharged (Figure 4c & Figure S4). However, the situation changes under a fast charge-discharge regime. As seen LLMO−1c and LLMO−2c showed better capacity retention than the LLMO-PVDF at 1 C and higher charge-discharge rates (Figure 4c). The LLMO−2c electrode showed excellent charge-discharge characteristics at 5 C and 10 C, with a retained capacity of 74 and 68 mAh/g, respectively. Hence, the **2c** binder has a more positive effect on the C-rate of the cathode and lower ICE loss than the others (1c and PVDF), which is also reflected in the cycling stability. Figure 4d shows the 200 times cycling result of LLMO−1c, LLMO−2c, and LLMO-PVDF electrodes at C/5 rate after the first charging, *i.e.*, ICE loss. The LLMO−2c electrode performed very well in cycling at 0.2 C with an excellent retained capacity of 184 mAh/g after 200 cycles, maintaining 89.3% of its 206 mAh/g initial capacity. In comparison, the LLMO−1c electrode started with a slightly higher specific capacity of 210 mAh/g and lost 60 mAh/g of its capacity after 200 cycles which corresponds to 71.43% capacity retention. However, the LLMO-PVDF cathode showed a final capacity of 134 mAh/g after 200 cycles which corresponds to 64.7% capacity retention. The capacity fade of the LLMO cathodes is related to the gradual growth of the spinel phase, which also results in voltage fade cycle by cycle.[10] The voltage fade can be observed from the GCD curves of the cathodes during the cycling stability tests. According to Figure S5, the discharge voltage fade of LLMO-PVDF is higher than the LLMO−1c and LLMO−2c whilst the LLMO−2c shows the lowest voltage fade and thus represents better cycling stability. For example, the discharge voltage of LLMO-PVDF at the half-specific capacity (~100 mAh/g) was 3.51 V in the first discharge, which decreased to 2.99 V in the 200th cycle, corresponding to a voltage fade of

0.52 V (Figure S5). In contrast, at the same specific capacity, the LLMO−1c showed a slightly better voltage fade of 0.39 V (3.61 V@1st and 3.22 V@200th cycle) whereas the LLMO−2c showed the lowest voltage fade of 0.24 V (3.59 V@1st and 3.35 V@200th cycle) after 200 cycles. Consequently, the **2 c** binder should be suppressing the growth of the spinel phase more than the others. If the reason behind the higher cycling stability and C-rate performance of LLMO−2c compared to LLMO−1c and LLMO-PVDF is its morphological features, then this needs further proof. We, therefore, used SEM, EDX and XRPD techniques on cycled and uncycled electrodes to investigate the morphology change and thus gain more information about the effect of different binders on the cell performance. The PPy was synthesized with different oxidants, *i.e.*, NaPS or APS, and it can be seen that there was no obvious difference in the morphology of the resulting PPy in the SEM images (Figure 5). However, in the case of the polymerization of pyrrole inside the PSAP solution, the initiator affected the morphology of the resulting material. As can be seen from the SEM images (in the first column of Figure 5), the **1 c** showed a very rough surface similar to PPy prepared by either the presence of NaPS or APS whereas the APS-initiated **2 c** showed a very smooth surface. On the other hand, uncycled LLMO−1c and LLMO−2c represent a similar morphology of distributed LLMO crystals bound by the **1 c**&**2 c** whereas the LLMO-PVDF shows a slightly smaller diameter of LLMO crystal shapes (Figure 5, 2nd column). The difference in the morphology of the LLMO-PVDF compared to LLMO−1c&LLMO−2c may come from the difference in the preparation process. The LLMO-PVDF cathode was prepared in NMP whereas the LLMO−1c&2c cathodes were prepared in environmentally friendly and green solvent, water.

The most prominent change in the SEM images was observed for the cycled cathode materials (LLMO-PVDF, LLMO−1c and LLMO−2c, on the 3rd column of Figure 5). The cycled and uncycled LLMO-PVDF has an obvious difference and visible change in the morphology after 200 cycles (Figure 5). It looks LLMO-PVDF cathode lost most of the active crystalline LLMO particles after cycling and left behind a cathode material covered by the binder, which may cause an extra decrease of capacity by blockage of the mass transfer. On the other hand, the LLMO−1c and LLMO−2c cathodes do not have this negative effect in the SEM images after cycling (Figure 5). Besides, the SEM images of the LLMO−1c and LLMO−2c cathodes on a wider scale show that they have a more porous surface either before or after cycling compared to LLMO-PVDF (Figure S6). This reminds a higher electrode surface area and thus may result in a better cell performance. We did not observe any cracks on the surface of cycled LLMO−1c and LLMO−2c on wider scales in contrast to cycled LLMO-PVDF has some cracks as it was reported in the literature (Figure S6).[11] However, a slight partial change on the surface of LLMO−1c appeared after cycling (Figure 5). Most of the crystals in LLMO−1c remained almost the same whilst some of them were covered by some other materials after the cycling, which may be responsible for the capacity and further voltage fade as already observed in Figure 4d and other electrochemical measurements (Figure S2 and Figure S5). The coverage of the active material by some insulators may result in the blockage of the mass and charge transfer whilst loss of Li ions into the electrochemically inactive tetrahedral positions results in a voltage fade and thus further capacity loss. As it was proved from the impedance analysis, the LLMO−1c has much more R_{ct} (92.35 vs. 23.95 Ω) and mass transfer resistance than the LLMO−2c. However, the 1c binder has still improved conductivity, due to the presence of conductive PPy in its structure compared to LLMO-PVDF which might be one of the reasons for a better capacity retention of LLMO−1c in the cycling tests. On the other hand, a comparison of the cycled and uncycled SEM results of the LLMO−2c electrode shows an unchanged morphology, unlike the LLMO−1c and LLMO-PVDF, which might be the reason for the excellent discharge and cycling stability features of LLMO−2c (Figure 5). This is also clearly supported by the EDX analysis as represented in Figure 6.

The LLMO has its corresponding element peaks, *i.e.*, Mn, Ni, Co, C and O, in the EDX result mostly arising from the Kα and Kβ radiations (Figure 6). There was no difference between the cycled and uncycled samples of LLMO-PVDF in the EDX result

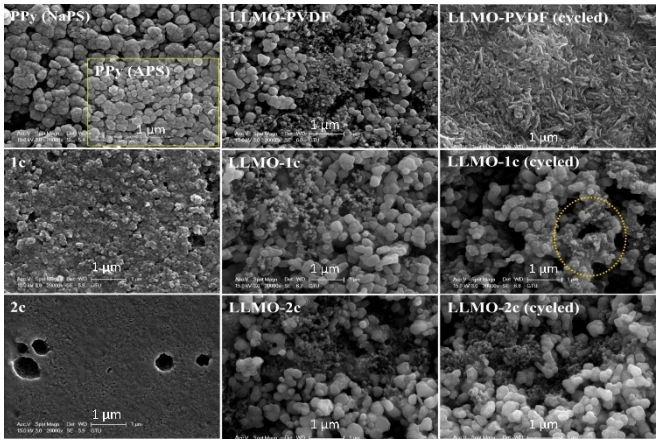

Figure 5. SEM images of PPy, **1 c**, **2 c** and cycled and uncycled LLMO-PVDF, LLMO−1c and LLMO−2c cathode materials.

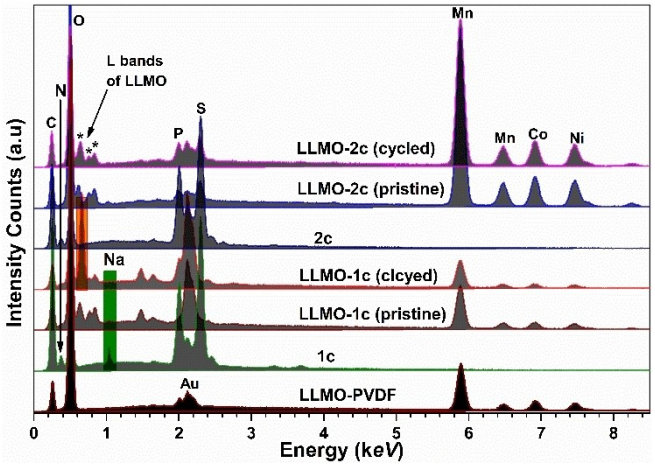

Figure 6. EDX analysis of cycled and uncycled LLMO-PVDF, LLMO−1c and LLMO−2c cathode materials.

except for the intensity ratio of the active material peaks to binder peaks. The composite binders **1c** and **2c** have their corresponding element peaks (P, S, N, C and O), confirming the existence of PPy and PSAP in their structures. The uncycled LLMO−1c and LLMO−2c cathode materials have the Kα and Kβ radiations arising from their parents as expected. Moreover, these uncycled LLMO−1c and LLMO−2c have additional bands arising from the L shell radiations of LLMO elements which probably arise from the interaction of the conductive PPy in the structures of these binders (**1c**&**2c**) with the active cathode material. Contrary to this, neither the cycled nor uncycled LLMO-PVDF has these additional bands confirming the interaction of binder with LLMO in LLMO−1c or LLMO−2c. The most prominent difference in the EDX result can be observed between the cycled and uncycled state of LLMO−1c. The intensity of the Mn L band increases abruptly when the LLMO−1c cycled whilst the intensity of Mn Kα and Kβ bands decreases (Figure 6). Since NaPS was used for the preparation of the 1c the Na Kα peak at 1.04 eV was also present in the EDX result (Figure 6). However, the intensity of this peak decreased in the uncycled LLMO−1c and almost disappeared in the cycled LLMO−1c. These changes further support that the **1c** binder interacted with the active LLMO material during the cathode preparation, and its structure probably changed into another material during the cycling (Figure 6). These possible structural interactions and changes were finally investigated by the XRPD analysis of the cathode materials. Figure 7 shows the comparative XRPD of uncycled and cycled cathode materials. The active cathode material $Li_{1.2}Mn_{0.54}Ni_{0.13}Co_{0.13}O_2$ (LLMO), prepared by the sol-gel method has its characteristics diffraction peaks at 2θ = 18.7° (003), 36.9° (101), 44.7° (104), 48.9° (105), 58.9° (107), and 68.8° (113) confirming the *O3* type layered structure based on hexagonal α–$NaFeO_2$ with space group of *R3m*.[51,52] Furthermore, the superlattice peaks between the 2θ = 20–22° correspond to the ordering of Li and Mn atoms in the transition metal layers of the Li_2MnO_3 component with a space group of *C/2m*.[53] The split peak couples at 2θ = 37.9°(006)&38.6° (012) and 64.6° (108)&65.5° (110) also show the well-layered structure.[53]

The cycled LLMO-PVDF has odd peaks at 2θ = 30.0°, 31.9° and 33.6° revealing the existence of $LiOH.H_2O$ which is one of the decomposition products of active LLMO cathode material and might be responsible from the capacity fade of the cell during the cycling.[54] The LLMO−1c and LLMO−2c have the characteristics peaks arising from the active cathode component in their pristine (uncycled) form. The LLMO−2c has all the expected layered structural peaks in the pristine state and their intensity does not change too much after cycling, which proves the high structural stability of the electrode. In contrast, the LLMO−1c does not have the signs of layered structural peaks in either cycled or uncycled form reminding an ordinary unlayered cathode material which also supports the EIS findings in Figure 4a. Furthermore, the cycled LMMO−1c has an interesting strong odd peak at 2θ = 14.2° whilst none of the other cathode materials have this odd peak except the uncycled LLMO−1c. Among the conductive binders used in this study, only **1c** was prepared in the presence of NaPS. Therefore, this peak can be assigned to the existence of different sodium manganate ($Na_xMn_yO_z$) structures in the cycled LLMO−1c cathode material.[55] The structure of $Na_xMn_yO_z$ is rather complex and has three different coordination places for five different Mn sites in a square-pyramidal geometry, which may be responsible for the comparatively higher capacity loss of LLMO−1c. Although it was speculated that the Na^+ ions in water-soluble binders could occupy lithium vacancies in the crystal structure of LLMO during cycling and are thus expected to play an essential role as a pillar in the lithium layer, leading to good structural stability, our findings do not support this hypothesis.[12] Unlike the CMC–Na or SA binders which are the source of the above hypothesis, the cation-binding ability and ionisation strength of PSAP [polybis(4-oxybenzene sulfonic acid)phosphazene] is quite different. Thus, the presence of highly ionisable Na^+ ions in the structure of **1c** results in the disruption of the layered structure of LLMO during electrode preparation. This also explains the presence of an unexpected peak ($Na_xMn_yO_z$) at 2θ = 14.2° in the XRPD result of LLMO−1c, and the abnormal intensity increase of the L band peak of Mn in the EDX spectra of cycled LLMO−1c. Hence, it can be concluded that the LLMO−1c electrode has a different morphology, even does not have a layered structure according to XRPD results. Therefore, LLMO−1c shows decreased cycling stability compared to the LLMO−2c which has the **2c** binder prepared in the presence of APS. Although it is inevitable to prevent layered to spinel phase transformation of the Li_2MnO_3 after the first charge, the high stability of LLMO−2c must originate from the improved electronic conductivity of the cathode ensured by the PPy component of the binder.

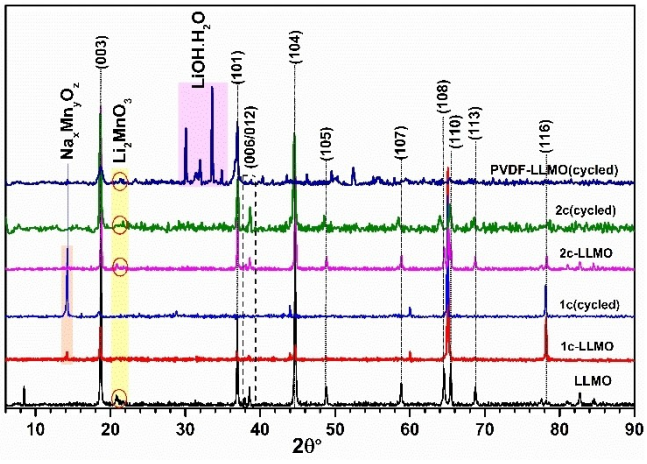

Figure 7. XRPD analysis of cycled and uncycled LLMO-PVDF, LLMO−1c and LLMO−2c cathode materials.

Conclusions

In summary, conventional polymer binder PVDF used in LIBs suffers from poor conductivity and requires the preparation of the electrode in toxic solvent *N*-methyl-2-pyrrolidone, which is

significantly undesirable for environmental aspects. Herein, we have successfully synthesized a series of water-soluble PPy/PSAP-based binders and investigated their effect on the electrochemical performance of $Li_{1.2}Mn_{0.54}Ni_{0.13}Co_{0.13}O_2$ (LLMO) cathode material. The cathode prepared by using the traditional PVDF binder showed an ICE loss of 98.6 mAh/g which is just 3.7 mAh/g lower than the cathode prepared by using **1c** binder (102.3 mAh/g). In contrast, the LLMO−1c electrode showed better capacity retention and cycling stability than the LLMO-PVDF after 200 cycles at a C/5 rate revealing the importance of enhanced conductivity provided by PPy. However, the XRPD analysis of either uncycled or cycled LLMO−1c electrode suggests that it does not have a layered structure, which was probably disrupted during the electrode preparation due to the presence of Na^+ ions in the structure of **1c** arising from the oxidant NaPS. On the other hand, the **2c** composite binder does not have this negative feature and provides good water solubility which allows the preparation of LLMO−2c electrode in a more environmentally friendly and greener way. The SEM, EDX and XRPD analyses show that the morphology of the LLMO−2c cathode remained almost unchanged after cycling. The LLMO−2c cathode showed excellent capacity retention of almost 90% after 200 cycles with an ICE loss of 74 mAh/g, surpassing the performance of LLMO-PVDF and LLMO−1c. The above electrochemical performance of LLMO−2c is also very comparable with the other water-based binders such as CMC–Na, XG, SA and PAA–Li.[10,12,13] These results can be attributed to the presence of additional electrical conductor PPy in the structure of **2c** binder whereas the CMC–Na, XG, PAA–Li and SA binders can only provide ionic conduction. The synergy between the electronic conductor PPy and high ionic conducting PSAP results in a low charge transfer resistance of ~24 Ω for LLMO−2c, compared to other binders such as CMC–Na (134.05 Ω), PVDF (148.0 Ω), and Polyacrylonitrile (78.48 Ω).[13] As a result, all these features of the **2c** bring enhanced LLMO stability which leads to good cycling stability, high C-rate and high capacity retention and is quite promising for the development of high-performance LLMO-based LIBs.

Experimental Section

Materials

PCl_5, THF, toluene, lithium acetate dihydrate ($C_2H_3LiO_2 \cdot 2H_2O$), nickel acetate tetrahydrate ($C_4H_6NiO_4 \cdot 4H_2O$), cobalt acetate tetrahydrate ($C_4H_6CoO_4 \cdot 4H_2O$), manganese acetate tetrahydrate ($C_4H_6MnO_4 \cdot 4H_2O$), and Ammonium hydroxide (NH_4OH) were purchased from Sigma-Aldrich and used as received. The deuterated solvent, D_2O for NMR spectroscopy, NaH (60% suspension in mineral oil), ethanol, citric acid monohydrate ($C_6H_8O_7$), and HCl (37%) were obtained from Merck. Sodium peroxydisulfate (98%) (NaPS), ammonium peroxydisulfate (98%) (APS) and polyvinylidene difluoride (PVDF, Mw = 530 kDa.) were obtained from Alfa Aesar. 1,1,1,3,3,3-hexamethyldisilazane (HMDS) (98%) and Pyrrole (98%) (B.p. 128–129 °C) were distilled and sealed under argon before use. All other reagents and solvents were reagent-grade quality and obtained from commercial suppliers.

Equipment

FT-IR spectra were recorded on a Bruker Alpha-P in ATR in the range of 4000–650 cm^{-1}. ^1H and ^{31}P NMR spectra were recorded in D_2O solutions on a Varian 500 MHz spectrometer. The thermal properties of the compounds were investigated on Mettler Toledo TGA/SDTA 851 thermogravimetric analysis (TGA) and differential scanning calorimeter DSC 821^e (DSC) equipped with Mettler Toledo Star^e software at a heating rate of 10 °C min^{-1} under nitrogen flow (50 mL min^{-1}) between 25–700 °C. The XRPD of the samples were carried out by using a fully automated Rigaku Smartlab X-ray diffractometer and recorded in the 2θ range of 5°–90° using Cu Kα radiation (λ = 1.5406 Å). The SEM images of polymers were taken in a Philips XL30 SFEG operated at 15 kV. UV–Vis spectra of the samples were recorded at room temperature on an Ocean Optics MAYA 2000pro in the range of 300–1100 nm in 50 ppm water solutions. Radical properties of composites were investigated on a Jeol JES FA 300 X-band (9.15 GHz) EPR spectrometer. The temperature-dependent DC conductivity properties of 13 mm diameter pressed pellets of the PPy, **1a–c** and **2a–c** composites were measured by using a Hioki IM3536 LCR meter in the DC mode in a two-probe electrode setup where the sample temperature was controlled by a precision (±0.1 °C) temperature control system (Heges Kimya LTD.) by 10 °C intervals between 20–100 °C. The DC (σdc) conductivities were calculated from the following equation (1);

$$\sigma_{dc} = l/(R_{dc} * A) \quad (1)$$

where σ_{dc} is the DC conductivity, l is the thickness of the sample (cm), R_{dc} is the measured resistance (Ω), and A is the area (1.3273 cm^2) of the sample.

Battery Fabrication

The active cathode material ($Li_{1.2}Mn_{0.54}Ni_{0.13}Co_{0.13}O_2$, LLMO) was prepared according to the literature procedure.[42] The working electrodes were fabricated by mixing active material (LLMO), acetylene black and binder in water with a mass ratio of 8:1:1 to form a homogeneous slurry, which was then coated onto an aluminium foil with a doctor blade and dried in a vacuum oven at 65 °C for 12 h. A similar procedure was also followed for the preparation of cathode material with PVDF binder. In this case, LLMO, acetylene black and PVDF were mixed in *N*-methyl-2-pyrrolidone (NMP) for cathode slurry preparation. The dried electrodes were cut into 2032-coin cell disks and then the cells were assembled in an argon-filled glove box with lithium foil as counter electrode and porous polypropylene film (T-PP-8 from Xiamen Tob New Energy Technology Co., Ltd.) as separator. The electrolyte was 1 M $LiPF_6$ in a mixture of ethylene carbonate/diethyl carbonate (EC/DEC) with a volume ratio of 1:1.

Electrochemical Measurements

The galvanostatic cycling of the cells was performed on the NEWARE program-controlled test system (Shenzhen, CT-2001 A, China) between 2.8 to 4.6 V (vs. Li/Li^+) with a current density of 0.2 C (1 C = 250 mAh/g) at room temperature. The electrochemical characterizations (EIS & CV) of cells were performed on a Gamry Reference 3000 electrochemical workstation. The electrochemical impedance spectroscopy (EIS) of the prepared cells was measured in the frequency range of 1 MHz to 1 mHz at the open circuit voltage. The cyclic voltammetry (CV) measurements of the electrodes (LLMO-PVDF, LLMO−1c and LLMO−2c) were performed at a

Table 2. Used reagent amounts for preparation of PPy/PSAP composites.

Composite	APS (mg)	NaPS (mg)	Pyyrole (mg)	PSAP (mg)	Ratio (eq./eq.)
1a		54.0	14.3	150	0.49:1.00
1b		105.4	26.1	150	0.99:1.00
1c		158.1	39.1	150	1.49:1.00
2a	52.6		14.3	150	0.49:1.00
2b	102.0		26.1	150	0.99:1.00
2c	153.0		39.1	150	1.49:1.00

scanning rate of 0.1 mV/s in the voltage range of 2.0 to 4.7 V using Li/Li^+ counter electrode.

Synthesis

The precursor monomer N-silylphosphoranimine ($Cl_3P{=}NSiMe_3$) was synthesized and purified by vacuum distillation according to the literature procedure[43] and then polymerised to polydichlorophosphazene (PDCP) in DCM (100 ml) with an initiator (PCl_5, 5.9 mg, 0.028 mmol) to monomer ($Cl_3P{=}NSiMe_3$ 2.24 g, 10.0 mmol) ratio of 1:350 (Scheme 1).[44] $\{^1H\}^{31}P$ NMR ($CDCl_3$) $\delta = -17.6$ ppm (br s, 1P, $(Cl_2PN)_n$). The polydichlorophosphazene was then isolated by removal of the volatiles, washed with 100 mL of hexane two times and it was dissolved in 50 mL of dry THF to react with the small excess of ethyl 4-phenol sulfonate ester (4.45 g, 22.0 mmol) in the presence of NaH (0.88 g, 22.0 mmol). The reaction was completed in 24 hours and the resulting crude polymer was then subsequently hydrolysed to polybis(4-oxybenzene sulfonic acid)phosphazene (PSAP) and purified as described previously.[41] $\{^1H\}^{31}P$ NMR (D_2O) $\delta = -20.11$ ppm [br s, $P(OPhSO_3H)_2$]. ^1H NMR (D_2O) $\delta = 6.55$ and 7.35 ppm [two br s, aromatic phenyl protons]. GPC: $Mw = 2.31\times10^5$, PDI = 1.34.

Synthesis of Polypyrrole

Polypyrrole (PPy) was synthesized for comparison of the electronic and morphological properties with the composites developed in this study. In a typical process, freshly distilled pyrrole was dissolved in water to obtain a 0.1 M aqueous solution and then mixed with a 0.125 M ammonium persulfate (APS) or sodium persulfate (NaPS) solution in a 100 mL flask by 1:1 (v/v) ratio. The resulting reaction mixture was kept below 5 °C by immersing the reaction flask in the ice-salt bath. A change of colour from greenish to black was observed. Then the reaction was completed after being kept on a stirrer for 24 h at room temperature. The synthesized PPy was collected by filtration and thoroughly washed with distilled water, methanol, and acetone to remove the oligomers. The washing procedure was repeated until the washing solution became colourless. The resulting PPy powder dried in a vacuum oven at 60 °C for 24 h and the samples obtained were characterized through various techniques.

Preparation of PPy/PSAP (1a–c&2a–c) composites

The synthesis of sulfonic acid substituted polyphosphazene (PSAP) and PPy composites with various pyrrole monomer feed ratios (with a fixed 1:1.25 monomer to oxidant ratio) was similar. In detail, PSAP (0.15 g) was initially added to a 50 mL round-bottomed flask containing 10 mL of distilled water at 0–5 °C and the mixture was stirred until the complete dissolution of PSAP. The pyrrole was added (1:0.5, 1:1, 1:1.5 mol/mol ratio of Pyrrole to PSAP) dropwise to the PSAP solution with continued stirring. During the mixing of pyrrole with the PSAP, a pyrrole-PSAP complex formed, and the colour changed into a slightly dark solution. Then the oxidant APS or NaPS solution in 10 mL of water (pyrrole/oxidant ratio of 1:1.25) was slowly added to the reaction mixture. The reaction turned dark black in 1 h and was allowed to stir overnight. The resulting dark black reaction mixture was then completely transferred into a dialysis membrane (cut off 2000 Da) and dialysed against distilled water for 3 days for the removal of unreacted pyrrole, oligomers, and salts. Dark black solutions obtained from the dialysis membrane were transferred into Teflon Petri dishes and dried in a vacuum oven at 60 °C overnight to yield **1a–c** and **2a–c** composites. The specific reaction conditions and used reagent amounts are given in Table 2.

Supporting Information

Comparative ^1H and ^{31}P NMR results of PSAP with **1b** and **2b**, CV results, Equivalent circuit model and analysis, GCD at different C-rates and different cycles, and SEM images of cycled and uncycled electrodes on a wider scale can be found in the Supporting Information.

Acknowledgements

We greatly acknowledge TUBITAK for funding our research under grant numbers 113Z314&118Z711 which led to the development of the materials used in this work. The post-doctoral bursary (2219) provided by TUBITAK to EBC (1059B192000291) is greatly acknowledged. We also would like to acknowledge Enwair Energy Technologies Corp. for allowing us to use their battery testing infrastructure.

Conflict of Interests

The authors declare no conflict of interest.

Data Availability Statement

The data that support the findings of this study are available from the corresponding author upon reasonable request.

Keywords: Polymer Composites · Polyphosphazene · Layered lithium rich cathode · Water-soluble binder · Lithium-ion battery

[1] D. Dai, B. Li, H. Tang, K. Chang, K. Jiang, Z. Chang, X. Yuan, *J. Power Sources* **2016**, *307*, 665.
[2] J. Song, B. Li, Y. Chen, Y. Zuo, F. Ning, H. Shang, D. Xia, *Adv. Mater.* **2020**, *32*, 2000190.
[3] Y. Liu, Z. Yang, J. Li, B. Niu, K. Yang, F. Kang, *J. Mater. Chem. A* **2018**, *6*, 13883.
[4] F. Fu, Y. Yao, H. Wang, G. L. Xu, K. Amine, S. G. Sun, M. Shao, *Nano Energy* **2017**, *35*, 370.
[5] B. Çetin, Z. Camtakan, N. Yuca, *Mater. Lett.* **2020**, *273*, 127927.
[6] H. Z. Zhang, Q. Q. Qiao, G. R. Li, X. P. Gao, *J. Mater. Chem. A* **2013**, *2*, 7454.
[7] S. Y. Kim, C. S. Park, S. Hosseini, J. Lampert, Y. J. Kim, L. F. Nazar, *Adv. Energy Mater.* **2021**, *11*, 2100552.
[8] Y. Chen, Y. Li, S. Tang, T. Lei, S. Deng, L. Xue, J. Zhu, *J. Power Sources* **2018**, *395*, 403.
[9] S. Hu, A. S. Pillai, G. Liang, W. K. Pang, H. Wang, Q. Li, Z. Guo, *Electrochemical Energy Reviews* **2019**, *2*, 277.
[10] S. Zhang, H. Gu, H. Pan, S. Yang, W. Du, X. Li, F. Pan, *Adv. Energy Mater.* **2017**, *7*, 1601066.
[11] Z. W. Yin, T. Zhang, S. J. Zhang, Y. P. Deng, X. X. Peng, J. Q. Wang, S. G. Sun, *Electrochim. Acta* **2020**, *351*, 136401.
[12] T. Zhao, Y. Meng, R. Ji, F. Wu, L. Li, R. Chen, *J. Alloys Compd.* **2019**, *811*, 152060.
[13] G. Zhang, B. Qiu, Y. Xia, X. Wang, Q. Gu, Y. Jiang, Z. He, Z. Liu, *J. Power Sources* **2019**, *420*, 29.
[14] M. Yu, Y. Wang, Z. Y. Wang, Y. P. Fan, J. H. Song, D. F. Zhou, J. Y. Xie, *J. Electrochem. Soc.* **2019**, *166*, A4122.
[15] T. H. Le, Y. Kim, H. Yoon, *Polymer* **2017**, *9*, 150.
[16] N. D. Gupta, S. Maity, K. K. Chattopadhyay, *J. Ind. Eng. Chem.* **2014**, *20*, 3208.
[17] R. Ansari, *E-Journal of Chemistry* **2006**, *3*, 186.
[18] V. A. Nguyen, C. Kuss, *J. Electrochem. Soc.* **2020**, *167*, 065501.
[19] A. Kassim, Z. B. Basar, H. E. Mahmud, *J. Chem. Sci.* **2002**, *114*, 155.
[20] S. Liu, T. J. Pan, R. F. Wang, Y. Yue, J. Shen, *Prog. Org. Coat.* **2019**, *136*, 105237277.
[21] R. B. Choudhary, S. Ansari, B. Purty, *J. Energy Storage* **2020**, *29*, 101302.
[22] P. Camurlu, *RSC Adv.* **2014**, *4*, 55.
[23] X. Tan, C. Hu, Z. Zhu, H. Liu, J. Qu, *Adv. Funct. Mater.* **2019**, *29*, 1903081.
[24] I. Sultana, M. M. Rahman, S. Li, J. Wang, C. Wang, G. G. Wallace, H. K. Liu, *Electrochim. Acta* **2012**, *60*, 201.
[25] A. Ramanavičius, A. Ramanavičienė, A. Malinauskas, *Electrochim. Acta* **2006**, *51*, 6025.
[26] P. Vahdatkhah, S. K. Sadrnezhaad, O. Voznyy, *J. Electroanal. Chem.* **2022**, *914*, 116317.
[27] R. Oriňáková, A. Fedorková, A. Oriňák, *Chem. Pap.* **2013**, *67*, 860.
[28] T. M. Wu, H. L. Chang, Y. W. Lin, *Polym. Int.* **2009**, *58*, 1065.
[29] C. Arribas, D. Rueda, *Synth. Met.* **1996**, *79*, 23.
[30] S. M. Dockheer, L. Gubler, P. L. Bounds, A. S. Domazou, G. G. Scherer, A. Wokaun, W. H. Koppenol, *Phys. Chem. Chem. Phys.* **2010**, *12*, 11609.
[31] S. M. Dockheer, L. Gubler, W. H. Koppenol, *Phys. Chem. Chem. Phys.* **2013**, *15*, 4975.
[32] L. Gubler, S. M. Dockheer, W. H. Koppenol, *J. Electrochem. Soc.* **2011**, *158*, B755.
[33] E. B. Çelebi, N. Demirhan, F. Hacıvelioğlu, *J. Mater. Chem. C* **2018**, *6*, 2672.
[34] F. Hacıvelioğlu, N. Kılıç, E. B. Çelebi, S. Yeşilot, *Polymer* **2016**, *96*, 112.
[35] H. R. Allcock, *Soft Matter* **2012**, *8*, 7521.
[36] H. R. Allcock, F. W. Lampe, J. E. Mark, H. R. Allcock, *Contemporary Polymer Chemistry*, Englewood Cliffs, NJ: Prentice-Hall, **2019**, p. 128.
[37] S. Ahn, H. S. Kim, S. Yang, J. Y. Do, B. H. Kim, K. Kim, *J. Electroceram.* **2009**, *23*, 289.
[38] M. T. Benson, M. K. Harrup, K. L. Gering, *Comput. Theor. Chem.* **2013**, *1005*, 25.
[39] S. Zhang, S. Li, Y. Lu, *eScience* **2021**, *1*, 163.
[40] X. He, S. Schmohl, H. D. Wiemhöfer, *ChemElectroChem* **2019**, *6*, 1166.
[41] E. B. Çelebi, F. Hacıvelioğlu, *Polym. Chem.* **2017**, *8*, 3022.
[42] S. Li, Y. Liang, D. Lei, Y. Xie, L. Ai, J. Xie, *AIP Conf. Proc.* **2018**, *1*, 020047.
[43] E. B. Çelebi, F. Hacıvelioğlu, *New J. Chem.* **2021**, *45*, 19364.
[44] H. R. Allcock, S. D. Reeves, C. R. De Denus, C. A. Crane, *Macromolecules* **2001**, *34*, 748.
[45] S. T. Navale, A. T. Mane, A. A. Ghanwat, A. R. Mulik, V. B. Patil, *Measurement* **2014**, *50*, 363.
[46] K. R. Jennings, *Spectrometric identification of organic compounds*, RM SILVERSTEIN, Wiley, **1991**, p. 430.
[47] M. Peo, H. Förster, K. Menke, J. Hocker, J. A. Gardner, S. Roth, K. Dransfeld, *Solid State Commun.* **1981**, *38*, 467.
[48] S. Maruthamuthu, J. Chandrasekaran, D. Manoharan, R. Magesh, *J. Polym. Eng.* **2017**, *37*, 481.
[49] F. Zheng, C. Yang, X. Xiong, J. Xiong, R. Hu, Y. Chen, M. Liu, *Angew. Chem. Int. Ed.* **2015**, *54*, 13058.
[50] D. Luo, X. Ding, J. Fan, Z. Zhang, P. Liu, X. Yang, Z. Lin, *Angew. Chem. Int. Ed.* **2020**, *59*, 23061.
[51] G. Wang, X. Wang, L. Yi, R. Yu, M. Liu, X. Yang, *J. Mater. Chem. A* **2016**, *4*, 15929.
[52] D. Li, Y. Sasaki, K. Kobayakawa, Y. Sato, *J. Power Sources* **2006**, *157*, 488.
[53] N. H. Vu, P. Arunkumar, J. C. Im, D. T. Ngo, H. T. Le, C. J. Park, W. B. Im, *Journal of Materials Chemistry A* **2017**, *5*, 15730.
[54] S. J. Lee, H. J. Jang, J. T. Son, *Mater. Lett.* **2021**, *301*, 130281.
[55] S. Altin, S. Altundag, E. Altin, D. E. P. Vanpoucke, S. Avci, M. N. Ates, *J. Alloys Compd.* **2023**, *936*, 168138.

Manuscript received: December 2, 2023
Revised manuscript received: January 4, 2024
Accepted manuscript online: January 29, 2024
Version of record online: February 20, 2024

RESEARCH ARTICLE

Water-soluble polypyrrole-polybis(4-oxybenzene sulfonic acid) phosphazene-based composite binders allow the preparation of layered lithium-rich manganese oxide-based cathodes in an environmentally friendly and green way. They provide low charge transfer resistance due to the presence of conductive PPy in their formulation which leads to excellent capacity retention of almost 90 % even after 200 cycles and high C-rate performance.

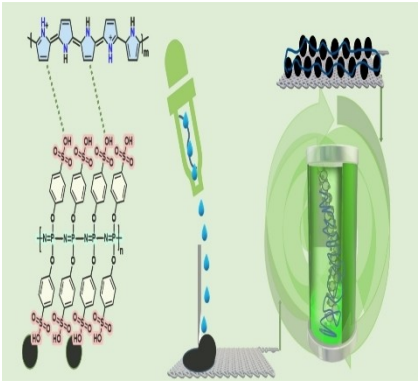

*H. Duyar, Dr. E. Büşra Çelebi, E. Güney, Prof. Dr. F. Hacıvelioğlu**

1 – 11

Water-soluble Polypyrrole-Polybis(4-oxy benzene sulfonic acid)phosphazene Composites and Investigation of Their Performance as Cathode Binder in Li-ion Batteries